Asian Journal of Chemistry; Vol. 37, No. 11 (2025), 2738-2744
ASIAN JOURNAL OF CHEMISTRY
https://doi.org/10.14233/ajchem.2025.34594

Enhanced Structural, Optical and Electrical Properties of Gd^{3+}-Doped $NiFe_2O_4$ Thin Films Synthesized by Spray Pyrolysis

VIKAS U. MAGAR[1,*], SAGAR RATHOD[1], TUKARAM SARAF[2], M.K. BABREKAR[3] and K.M. JADHAV[4]

[1]Department of Physics, Deogiri College, Chhatrapati Sambhajinagar-431001, India
[2]Twaritapuri Arts, Commerce and Science College, Talwada, Georai, Beed-431127, India
[3]Department of Physics, Indraraj Arts, Commerce and Science College, Sillod-431112, India
[4]School of Basic and Applied Sciences, M.G.M. University, Chhatrapati Sambhajinagar-431003, India

*Corresponding author: E-mail: vikasmagar3@gmail.com

Received: 1 August 2025 *Accepted*: 18 September 2025 *Published online*: 27 October 2025 AJC-22161

In this work, the successful synthesis and deposition of Gd^{3+}-doped nickel ferrite ($NiFe_{2-x}Gd_xO_4$, x = 0.00, 0.02, 0.04, 0.06, 0.08 and 0.10) thin films using the spray pyrolysis technique was achieved. The films were deposited onto ultrasonically cleaned glass substrates and subsequently annealed at 500 ºC for 4 h to enhance crystallinity and phase formation. This approach offers a cost-effective and scalable route for fabricating doped ferrite thin films with tunable properties for potential electronic and magnetic device applications. The X-ray diffraction pattern reflects the presence of diffraction planes (220), (311), (222), (400), (422), (511) and (440), which belonging to the cubic structure. XRD analysis proved that the thin films possess a cubic spinel structure with single-phase formation. The crystallite size calculated from the FWHM of the (311) plane was found to be in the range of 16 to 10 nm. The lattice constant increased from 8.334 Å to 8.388 Å on Gd^{3+} doping. AFM analysis of typical samples revealed a granular nature and surface roughness and skewness factor. The cubic spinel structure was also confirmed by Raman spectroscopy, which revealed the presence of five active modes. The I-V characteristic study revealed the ohmic nature, showing the resistivity of the order of 10^6-10^7 Ω-m. The optical band gap determined from the Tauc plot was in the range of 1.46 eV to 1.80 eV. The band gap increases with increase with Gd^{3+} doping.

Keywords: Lattice constant, Nickel ferrite, Optical band gap, Spray pyrolysis, Thin film.

INTRODUCTION

Ferrites are the magnetic oxides with tunable electrical, magnetic and optical properties, influenced by their composition, structure and synthesis method. They exist in spinel, hexagonal and garnet forms, and are widely used in sensors, data storage, high-frequency devices and catalysis [1]. Among these ferrites, spinel ferrite is a unique and widely studied material for many applications. It is represented by the chemical formula MFe_2O_4 (M = Co^{2+}, Ni^{2+}, Zn^{2+}, *etc*.) and possesses a cubic spinel structure with the space group fd_3mOh^7 [2-5]. The crystal structure of spinel ferrite consists of tetrahedral (A) and octahedral [B] sites, in which various types of cations are combined. The occupancy of the cations at (A) and [B] sites is important for understanding their structural, electrical, optical and magnetic properties. Spinel ferrite exhibits high electrical resistivity, low eddy current and dielectric losses, high saturation magnetization, high permeability and a high Curie temperature. The properties of ferrite are sensitive to its size, shape and morphology [6]. It is well-known that the properties of nano size spinel ferrite are superior to those of bulk spinel ferrite [7]. Nano-size materials exhibit extraordinary properties such as small size of the order of nanometer, large surface-to-volume ratios, biocompatibility, biodegradability and chemically more stability.

In recent years, nanocrystalline ferrite thin films have gained significant attention due to their large surface areas. Applications of ferrite thin films include data storage, transformers, batteries, gas sensors, magnetic recording medium, microwave devices and hydrogen production [8-14]. The properties exhibited by the thin film ferrite mostly depend on their preparation and deposition techniques [7]. Different deposition techniques are available, which are divided into two groups: (i) physical and (ii) chemical methods, such as pulse laser deposition (PLD), dip coating, sputtering and spray pyrolysis [15-18]. Among various deposition techniques, spray

pyrolysis is widely employed due to its simplicity, cost-effectiveness and ability to produce thin films with large surface area and good uniformity. This method requires low energy and good control of the size and thickness of the film. This method is also useful for producing mixed thin films of nanocrystalline nature [19].

Literature reports indicate extensive studies on nickel ferrite thin films doped with various divalent and trivalent cations [20-25]. However, systematic investigations on the influence of rare-earth ion doping particularly on the structural, Raman, morphological, electrical and optical properties remain limited. Among rare-earth elements, Gd^{3+} is of particular interest due to its strong magnetic moment and preferential occupation of octahedral [B] sites in the spinel lattice, which significantly alters material properties. Significantly, studies on Gd^{3+}-doped nickel ferrite thin films are scarce, highlighting the need for further exploration. Nickel ferrite is a promising candidate for various technological applications. It shows an inverse spinel structure with Ni^{2+} occupying mainly octahedral [B] sites and Fe^{3+} ions occupying both tetrahedral (A) and octahedral [B] sites. Therefore, an attempt is made to understand the influence of Gd^{3+} doping on the structural, morphological, Raman, electrical and optical properties of nickel ferrite thin films in nanocrystalline form grown by spray pyrolysis.

EXPERIMENTAL

The synthesis of $NiFe_{2-x}Gd_xO_4$ (where x = 0.00, 0.02, 0.04, 0.06, 0.08 and 0.10) thin films requires AR grade nickel nitrate hexahydrate ($Ni(NO_3)_2{\cdot}6H_2O$), gadolinium nitrate nonahydrate ($Gd(NO_3)_3{\cdot}9H_2O$) and ferric nitrate nonahydrate ($Fe(NO_3)_3{\cdot}9H_2O$). The molar ratio of the metal nitrate to iron nitrate was 1:2. The glass substrate was then carefully soaked in chromic acid for 40 min. These glass substrates were cleaned for 40 min in using acetone and finally with water before being utilized as glass substrates to deposit the thin films.

Thin film preparation: Using spray pyrolysis techniques $NiFe_{2-x}Gd_xO_4$ (x = 0.00, 0.02, 0.04, 0.06, 0.08 and 0.10) thin films were grown and deposited on clean glass substrate of dimensions of 75 mm × 25 mm × 1.35 mm. Analytical grade (purity ~99.98%) nickel nitrate hexahydrate ($Ni(NO_3)_2{\cdot}6H_2O$), nickel nitrate hexahydrate ($Ni(NO_3)_2{\cdot}6H_2O$), gadolinium nitrate nonahydrate ($Gd(NO_3)_3{\cdot}9H_2O$) and ferric nitrate nonahydrate ($Fe(NO_3)_3{\cdot}9H_2O$) were used. After dissolving each nitrate in deionized water, 0.1 molarity of each ion-Ni^{2+}, Gd^{3+} and Fe^{3+} was extracted. In a 1:2 volumetric ratio, the arranged solutions of ferric, gadolinium and nickel nitrates were combined (ferric nitrate was number two and nickel nitrate was number one). A spray gun was then used to spray the mixture of nickel nitrate and ferric nitrate over a glass substrate that had been preheated to approximately 385 ºC while using the proper nozzle pressure (0.26 pa). After each spray, it takes approximately around three to 4 min to reach the desired temperature, which is slightly lowered by the planned application. The temperature of substrate was maintained using a temperature controller. Table-1 lists the values of several optimized parameters that were maintained during the thin film deposition process, including the spray pressure to substrate distance rate. After the whole deposition process, the substrate temperature was maintained at a steady level for 12 to 18 min to allow the thin layer to form before gradually cooling to room temperature. Since water molecules and other contaminants may be eliminated from the sample at this temperature, the former thin film was annealed for 4 h at 500 ºC. A block diagram of the spray pyrolysis setup used to develop the $NiFe_{2-x}Gd_xO_4$ (x = 0.00, 0.02, 0.04, 0.06, 0.08 and 0.10) thin films is shown in Fig. 1.

TABLE-1
OPTIMIZED PARAMETERS OF SPRAY DEPOSITION OF $NiFe_{2-x}Gd_xO_4$ (x = 0.00, 0.02, 0.04, 0.06, 0.08, 0.10) THIN FILMS

Parameters	Specification
Molarity proportion	1:2
Volume proportion	1:2
Dimensions cleaned glass	(75 mm × 25 mm × 1.35 mm)
Nozzle to substrate distance	28 cm
Spray rate	2-4 mL/min
Spray pressure	0.26 Pa
Substrate temperature	385 ºC
Annealing temperature and time	500 ºC for 4 h

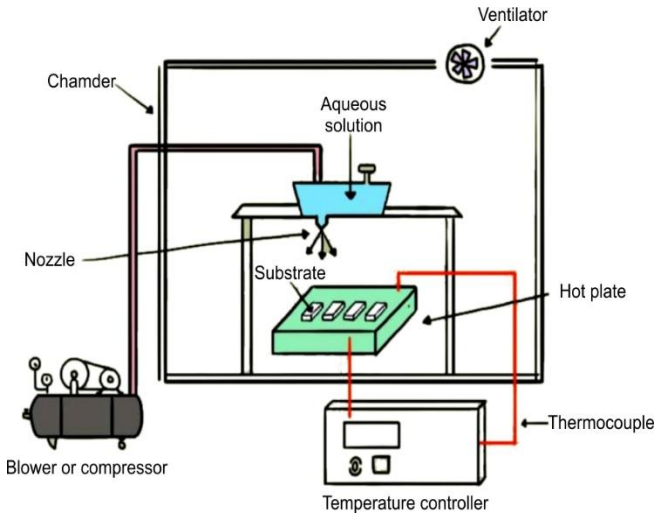

Fig. 1. Block diagram of the deposition of the thin film onto the glass substrate

Characterizations: Several characterization techniques were employed to evaluate the structural, electrical, optical and other properties of the Gd^{3+} doped nickel ferrite thin films. The XRD pattern of the BRUKER D8 advanced X-ray diffractometer was recorded. The structural features of the thin films were evaluated using Cu$K\alpha$ radiation in the 2θ range of 20º to 80º, to evaluate the structural features of the thin film. The surface morphology of the thin films was studied using AFM (Perk Systems; XE-7). The Raman spectra were recorded at room temperature using a STR-500 Micro-Raman Spectrometer. The I-V characteristics and the room temperature DC resistivity of the $NiFe_{2-x}Al_xO_4$ thin films were measured by a two-probe method using a Keithley source meter (Model No. 2400) with current measuring capability down to 10-13 ampere for the films in the metal-insulator-metal configuration. The optical absorbance of the films was measured on a Perkin-Elmer Lambda 950 UV-VIS spectrometer in the 200-800 nm wavelength range. The thicknesses of the Gd^{3+} doped nickel ferrite thin films were determined using the weight differences method.

RESULTS AND DISCUSSION

Thickness measurement: In this study, thin films of $NiFe_{2-x}Gd_xO_4$ (x = 0.00, 0.02, 0.04, 0.06, 0.08 and 0.10) were grown and deposited on a glass substrate. The thickness of the deposited thin films were calculated using the weight difference method. A glass substrate was used to deposit the thin films, whose weight were measured before and after deposition of the thin films. The weight was measured using an electronic balance with 0.01 mg accuracy. The thickness of the thin film depends on area, density and mass. The following relationship was used to calculate the thickness (t) of thin film and their value are listed in Table-2.

$$t = \frac{\delta m}{A\rho} \quad (1)$$

where δ represent density; m for mass; and A is the area of the films.

TABLE-2
VALUES OF THICKNESS (t), CRYSTALLITE SIZE (D), LATTICE CONSTANT (a), X-RAY DENSITY (d_x), VOLUME (V) OF $NiFe_{2-x}Gd_xO_4$ (x = 0.00, 0.02, 0.04, 0.06, 0.08, 0.10) THIN FILMS

Composition x	t (nm)	D (nm)	a (Å)	d_x (g/cm^3)	Volume (Å)^3
0.00	235	16	8.334	5.379	578.9
0.02	220	15	8.352	5.389	582.7
0.04	267	14	8.371	5.399	586.6
0.06	238	12	8.377	5.435	587.8
0.08	251	11	8.381	5.471	588.8
0.10	248	10	8.388	5.504	590.1

At room temperature, the X-ray diffraction patterns of aluminum-doped nickel ferrite ($NiFe_{2-x}Gd_xO_4$) are shown in Fig. 2. The observed reflections are indexed as (220), (311), (222), (400), (422), (511) and (540) by using Bragg's law. It is observed that all the reflections are sharp and slightly broader indicating the nanocrystalline nature. The XRD patterns are similar to other spinel ferrites reported in the literature and closely match with JCPDS card no. 08-0234 [26]. No additional reflection was observed in the XRD pattern indicating the single-phase nature. The complete analysis of the XRD pattern using the standard method confirms the cubic spinel structure associated with the thin films. The following relation was used to calculate the lattice constant [27]:

$$a^2 = \frac{\lambda^2(h^2+k^2+l^2)}{4\sin 2\theta} \quad (2)$$

The lattice constant of pure nickel ferrite closely agrees with the literature report [28]. The lattice constant gradually increases with the Gd^{3+} doping. The observed behaviour is analogous with the reported literature and can be justified with the help of the difference in ionic radii of Gd^{3+} and Fe^{3+} ions. The Fe^{3+} ions are replaced by doping of Gd^{3+}. The ionic radii of Gd^{3+} (0.93 Å) are greater than the ionic radius of Fe^{3+} (0.67 Å) ions and therefore the lattice constant increases with Gd^{3+} doping. These observations on lattice variation are in alignment with the results in the literature [29]. The unit cell volume (V) was evaluated using the lattice constant (a) and observed that

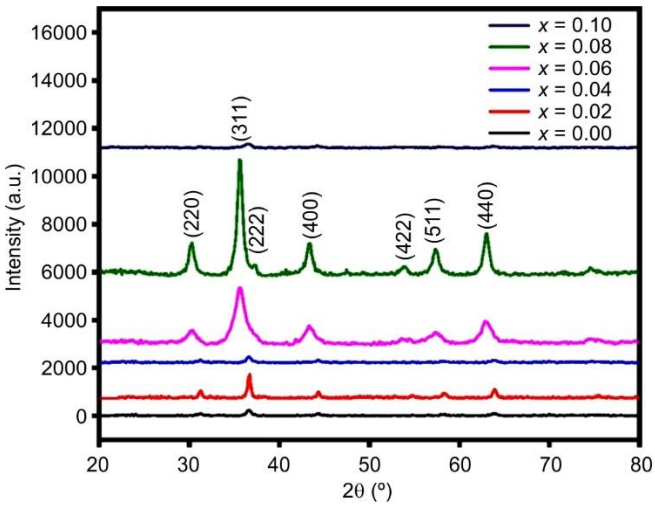

Fig. 2. X-ray diffraction pattern of $NiFe_{2-x}Gd_xO_4$ (x = 0.00, 0.02, 0.04, 0.06, 0.08, 0.10) thin films

unit cell volume increases with increases in Gd^{3+} doping (Table-2).

The X-ray density was calculated from the eqn. 3 [30]:

$$(\rho_x) = \frac{8M}{N_A a^3} \quad (3)$$

where m is the molecular weight; a is the lattice parameter of Gd^{3+} substituted nickel ferrite thin film; and N_A is Avogadro's number. Table-2 shows a decreasing trend in the X-ray density with increasing Gd^{3+} doping. The observed behaviour can be attributed to the increase in Gd^{3+} concentration x.

The Scherrer equation was used to calculate crystallite size, which is given by eqn. 4 [31]:

$$D = \frac{0.9\lambda}{\beta\cos\theta} \quad (4)$$

where λ is the wavelength; θ is Bragg's angle of diffraction; and β is the FWHM (Full width at half maxima). The obtained values are listed in Table-2. The microstructure parameters were calculated using the following relations [32-34]:

$$LS = \frac{\beta}{4\tan\theta} \quad (5)$$

$$\varepsilon = \frac{\beta\cos\theta}{4} \quad (6)$$

$$\delta = \frac{1}{D^2} \quad (7)$$

$$SF = \frac{2\pi^2}{45\sqrt{3\tan\theta}} \quad (8)$$

Table-3 displays the computed structural parameters. Lattice strain provides information on the deformation of the crystal lattice. Thermal expansion, contaminants, flaws, mechanical stress and other factors are typical causes. The lattice strain grew with increasing Gd^{3+} doping, validating the crystal lattice's deformation. Calculating the micro-strain allows to measure local deformation within the crystal's lattice. Table-3 shows that the micro-strain is rather modest and grows monotonically as the Gd^{3+} concentration increases. The reduced micro-strain readings confirm the uniform composition of the

TABLE-3
VALUES OF LATTICE STRAIN (LS), MICRO STRAIN (ε), DISLOCATION DENSITY (δ), STACKING FAULT (SF) FOR XRD PATTERNS OF $NiFe_{2-x}Gd_xO_4$ (x = 0.00, 0.02, 0.04, 0.06, 0.08, 0.10) THIN FILMS

x	LS	ε (× 10^{-3})	δ (× 10^{16} lines/m^{-2})	SF (×10^{-2})
0.00	4.847	1.439	41.54	0.429
0.02	5.442	1.518	43.80	0.427
0.04	5.338	1.571	45.34	0.431
0.06	5.190	1.537	44.36	0.430
0.08	5.090	1.537	44.35	0.426
0.10	5.102	1.537	44.34	0.427

manufactured materials. Dislocation density measures linear flaws in the crystallite when the atomic arrangement is not ideal. Table-3 shows that dislocation density increases with Gd^{3+} doping. Higher dislocation density values suggest a more defective lattice. Moreover, the stacking defect is caused by the irregularities in the usual stacking arrangements of atomic layers in the lattice. Currently, the stacking fault remains nearly constant, indicating that there is no substantial disruption in the atomic layers. As a result, predicted microstructural parameters increase with Gd^{3+} doping, except for the stacking defect, which remains nearly constant throughout the doping levels.

Atomic force microscopy: Fig. 3 shows the AFM images of typical samples of $NiFe_{2-x}Gd_xO_4$ (x = 0.00, 0.04 and 0.10). These images were used to study the surface topology of the thin film. The close analysis of the AFM images suggests the granular structure. The average roughness (Ra), root mean square roughness (Rrms), skewness (Sku) and Kurtosis (Rku) roughness parameter obtained from of AFM images are listed in Table-4 [35].

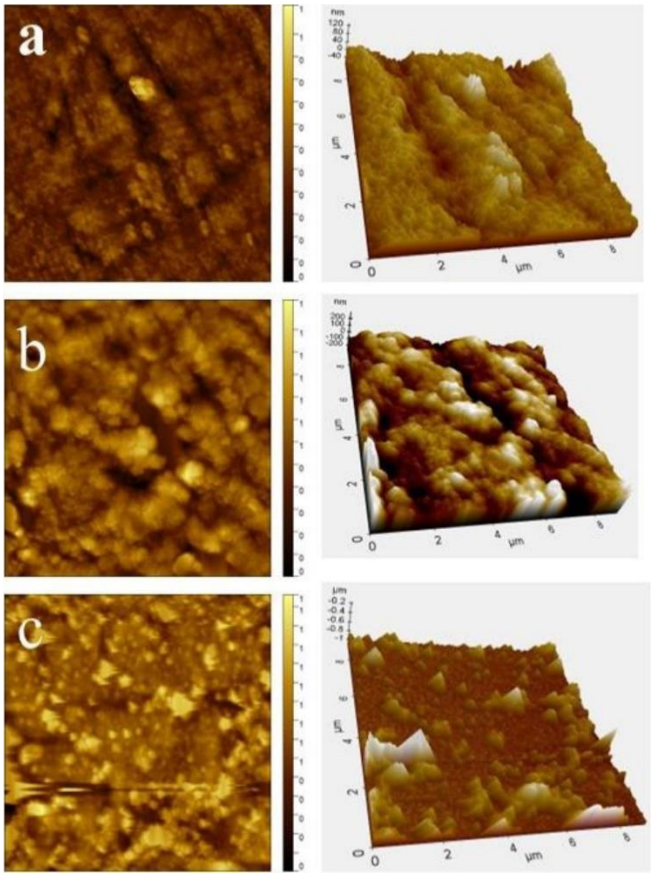

Fig. 3. 2-D and 3-D AFM images of $NiFe_{2-x}Gd_xO_4$ (x = 0.00, 0.04 and 0.10) thin films

TABLE-4
VALUE OF AVERAGE ROUGHNESS (Ra), ROOT MEAN SQUARE ROUGHNESS (R_{rms}), SKEWNESS (S_{ku}) AND KURTOSIS (R_{ku}) FOR AFM G^{3+} DOPED $NiFe_{2-x}Gd_xO_4$ (x = 0.00, 0.04, 0.10) THIN FILMS

x	R_a (μm) (± 0.01)	R_{rms} (μm) (± 0.01)	R_{sk} (± 0.01)	R_{ku} (± 0.01)
0.00	71.71	14.38	2.921	2.034
0.04	59.11	71.16	0.366	2.163
0.10	238.09	54.33	5.080	2.243

Raman spectroscopy: Usually, spinel ferrite shows five active modes instead of 42, which is according to the group theory. The Raman spectra for the thin films were recorded at frequency regions at 800-100 cm^{-1} and 300 K [36]. Raman spectra are shown in Fig. 4. A close examination of Raman spectra shows the presence of five active modes in A1g (R) + Eg (R) + T_{1g} (in) + 3 T_{2g} (R) + 2A_{2u} (in) + 2Eu (in) + 4 T_{1u} (IR) + 2T_{2u} (in) (1), where 'R', 'IR' and 'in' represent Raman and infrared vibrations and inactive modes respectively [37], which occurred at 691 cm^{-1}. These active modes can be divided into two regions, the high and low frequency regions. These active modes are attributed to the stretching mode metal-oxygen (M-O) bond at tetrahedral (A) and octahedral (B)2 sites. The incorporation of Gd^{3+} causes the shift of active modes towards low-frequency regions. The values of Raman active modes are listed in Table-5. In the prepared samples, the vibrational mode with Raman shift observed at approximately 702 cm^{-1} is assigned to A_{1g}, which originates from the metal-oxide bond in the tetrahedral site. The asymmetric stretching of Fe-O and Ni-O give the rise to the T_{2g} mode, which is a Raman shift at 474 cm^{-1}. The Raman shifts at 312 cm^{-1} is E_g mode corresponding to the symmetric bending of the oxygen atom with respect to the metal ion at a tetrahedral site. No trend was observed in the values of the Raman shift for A_{1g}, T_{2g} and E_g with Gd^{3+} substitution in nickel ferrite.

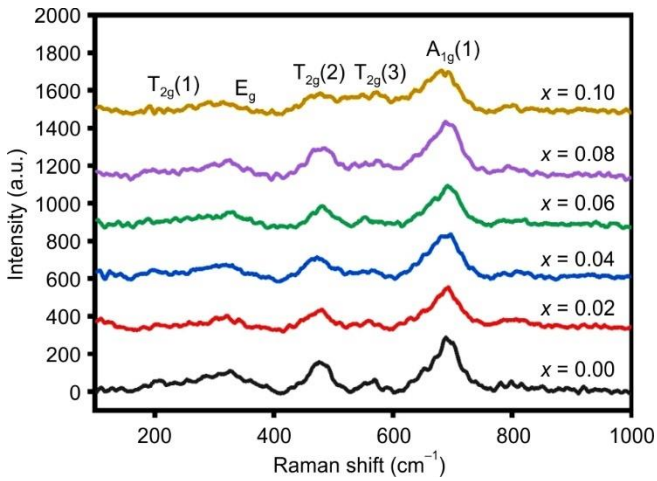

Fig. 4. Raman spectra of $NiFe_{2-x}Gd_xO_4$ (x = 0.00, 0.02, 0.04, 0.06, 0.08, 0.10) thin films

TABLE-5
VALUE OF RAMAN VIBRATION MODES OF $NiFe_{2-x}Gd_xO_4$ (x = 0.00, 0.02, 0.04, 0.06, 0.08, 0.10) THIN FILMS

x	$T_{2g}(1)$	E_g	$T_{2g}(2)$	$T_{2g}(3)$	$A_{1g}(1)$
0.00	208	324	476	569	691
0.02	206	320	479	557	693
0.04	202	323	471	564	696
0.06	204	330	481	552	692
0.08	203	327	486	574	688
0.10	201	319	477	576	679

Raman spectra confirmed the absence of any impurities in Gd^{3+} doped nickel ferrite thin films.

Current-voltage (I-V) characterization: The switching properties of the prepared thin films were studied using I-V measurements. A plot of current (I) and voltage (V) is shown in Fig. 5, which exhibits an almost linear relation. It is clear from the I-V plot that the thin film possesses high resistances exhibiting semiconductor behaviour. The thin films exhibit an ohmic nature, with resistance values in the order of mega ohm, are listed in Table-6. Gd^{3+} doping strongly influences the resistivity of pure nickel ferrite. The I-V plots were used to calculate the resistivity of the films using the following relations [36].

$$\rho = \frac{RA}{t} \quad (9)$$

where R is the resistance; A is the area of thin film; and t is the thickness of thin film. The resistivity values show an increasing trend with Gd^{3+} doping. The increase in resistivity can be attributed to 106-107 Ω-m increasing the concentration of Gd^{3+}. This increase in resistivity can be explained by the preferential tendency of Gd^{3+} to occupy either the A or B-site.

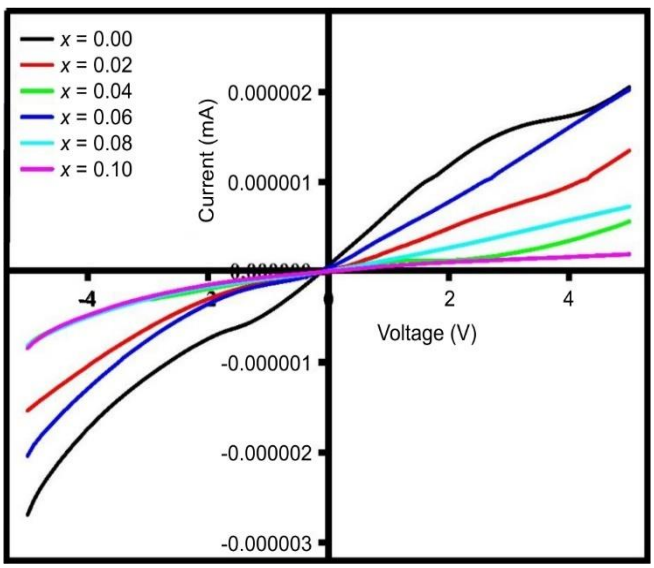

Fig. 5. I-V curves of $NiFe_{2-x}Gd_xO_4$ (x = 0.00, 0.02, 0.04, 0.06, 0.08, 0.10) thin films were recorded at room temperature

TABLE-6
RESISTIVITY OF $NiFe_{2-x}Gd_xO_4$ (x = 0.00, 0.02, 0.04, 0.06, 0.08, 0.10) THIN FILMS

Composition x	0.00	0.02	0.04	0.06	0.08	0.10
Resistivity (Ω-m)	2.78	3.04	3.57	2.68	2.98	3.58

Optical studies: The optical properties of the synthesized thin films were studied using the visible spectroscopy. Absorption spectra were recorded in the frequency range of 350 to 450 nm at room temperature Fig. 6. The absorption spectra revealed a hump-like structure, which varied with the Gd^{3+} doping. The absorbance coefficients were obtained from the absorbances spectra. The variation in $(\alpha h\nu)^2$ and photon energy is shown in Fig. 7 and is known as the Tauc plot. These Tauc plots were used to determine the band gap energy. The band gap energy values are listed in Table-7. The Tauc plot was used to calculate the band gap energy, considering the following relation [38]:

$$\alpha h\nu = A(h\nu - E_g) \quad (9)$$

here A is the Tauc parameter; hν is the photon energy; and E_g is the optical band gap energy.

TABLE-7
VALUE OF ENERGY BAND GAP (E_g) OF $NiFe_{2-x}Gd_xO_4$ (x = 0.00, 0.02, 0.04, 0.06, 0.08, 0.10) THIN FILMS

Composition x	0.00	0.02	0.04	0.06	0.08	0.10
Energy band gap, E_g (eV)	1.46	1.51	1.54	1.66	1.67	1.80

The band gap energy is influenced by several factors such as the lattice parameter, crystallite size, concentration, film thickness and the presence of impurities in the film sample. The Tauc relation was used to determine the energy bandgap as a function of incident photon energy. The observed energy bandgap obtained from 1.46 eV to 1.80 eV in ferrite materials can be affected by lattice defects, atomic displacement and grain boundary diffusion, especially in films prepared with larger deposition. It has been observed that the energy band gap increases with increasing Gd^{3+} concentration, which is attributed to the formation of new localized energy levels between the valence and conduction bands. This increase in bandgap is also associated with the expansion of the lattice constant owing to the substitution of Gd^{3+} ions.

Conclusion

Pristine nickel ferrite and Gd^{3+} was doped nickel ferrite thin films were effectively and uniformly deposited on a glass substrate using spray pyrolysis after the requisite parameters were adjusted. The thin films were produced with a uniform size and a nanocrystalline structure. X-ray diffraction analysis confirmed that the thin film was fabricated as a single phase with a cubic spinel structure. The variance in the ionic radii between Gd^{3+} and Fe^{3+} ions caused the lattice constant to increase when Gd^{3+} is doped. The structural parameter is also heavily impacted by Gd^{3+} doping. Raman spectra with five active modes reveal the cubic spinel structure of the thin film. The I-V characterization indicates that the resultant thin films were ohmic, with semiconducting behaviours. The band energy band fluctuates between 1.46 eV and 1.80 eV, supporting the semiconducting behaviour.

ACKNOWLEDGEMENTS

One of the authors, VUM, is grateful to the Mahatma Phule Research and Training Institute in Nagpur for their fellowship support and also grateful to the Director ICT Mumbai Marathwada Campus, Jalna, India for providing Raman data.

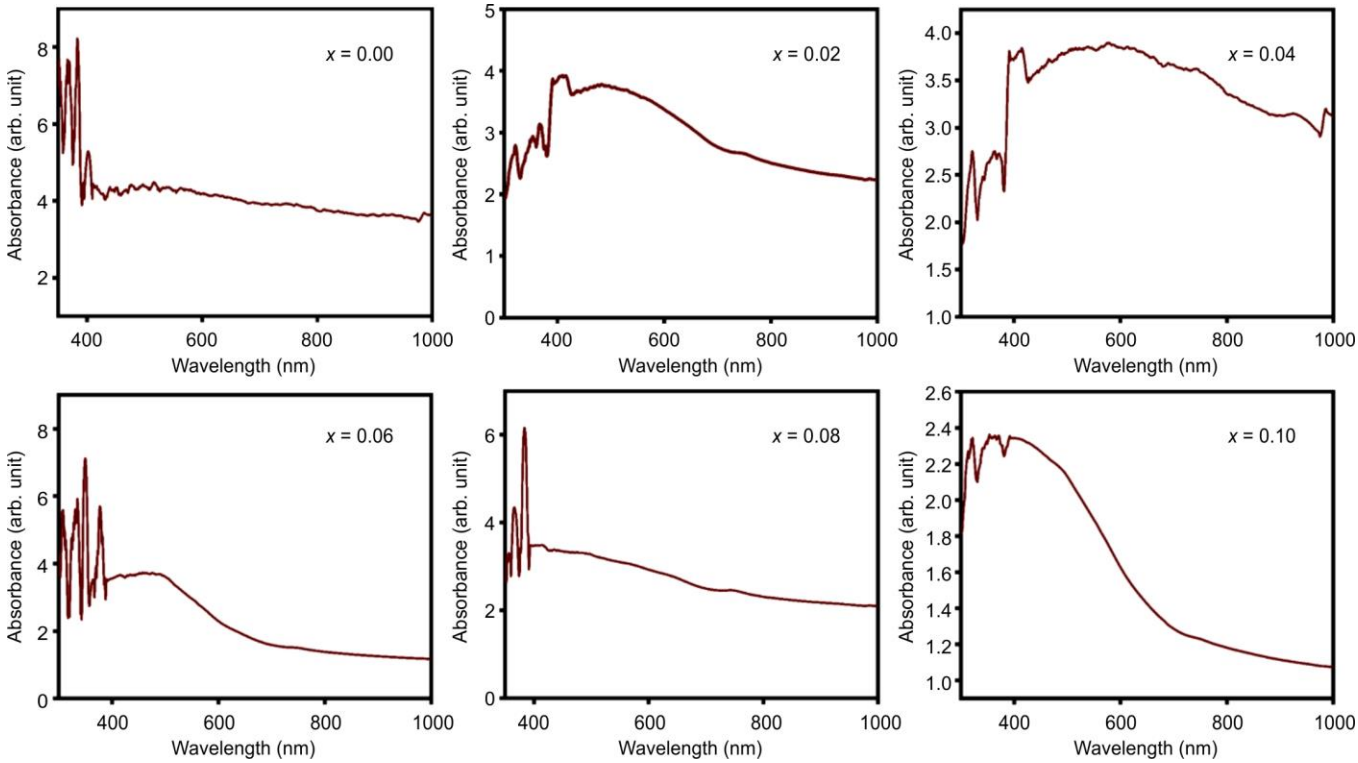

Fig. 6. UV-visible absorbance spectra of $NiFe_{2-x}Gd_xO_4$ (x = 0.0, 0.1, 0.2, 0.3 and 0.4) thin films

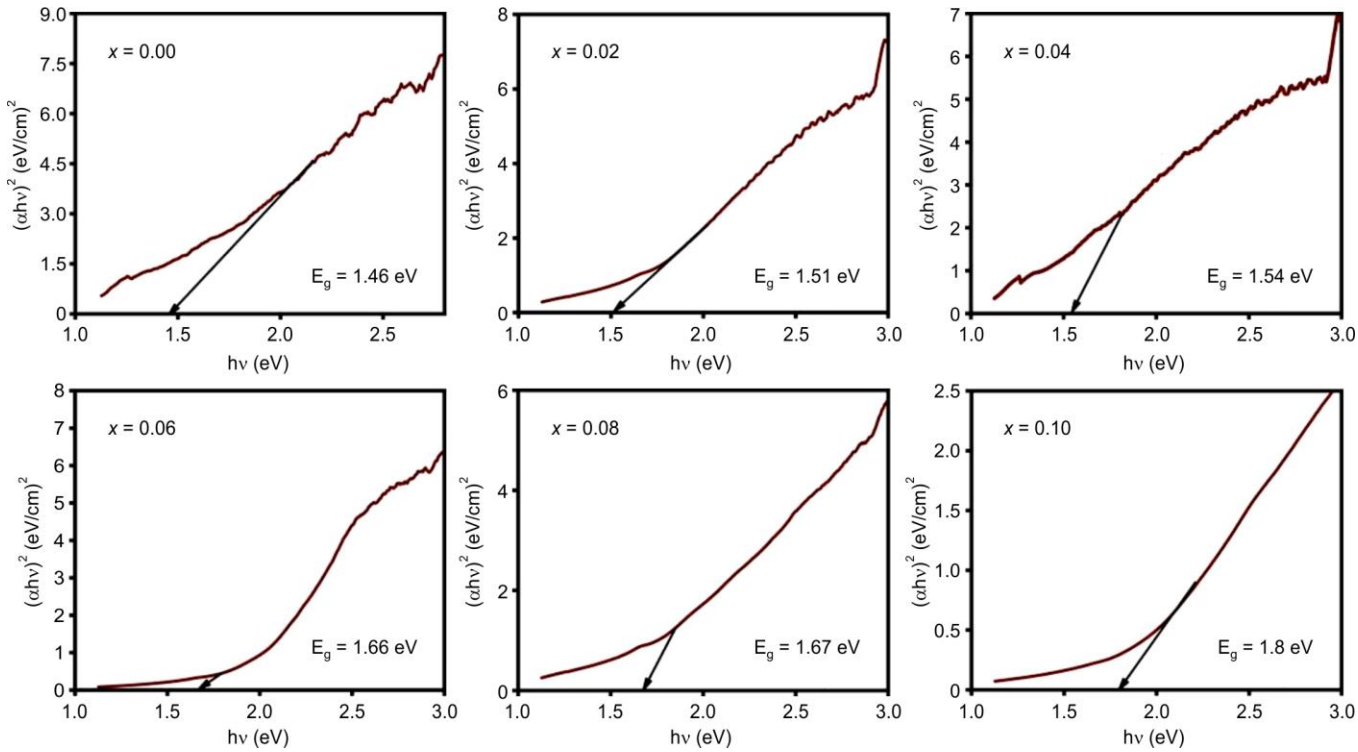

Fig. 7. Variation of $(\alpha h\nu)^2$ with photon energy ($h\nu$) of $NiFe_{2-x}Gd_xO_4$ (x = 0.00, 0.02, 0.04, 0.06, 0.08, 0.10) thin films recorded at room temperature

CONFLICT OF INTEREST

The authors declare that there is no conflict of interests regarding the publication of this article.

REFERENCES

1. S.F. Shaikh, M. Ubaidullah, R.S. Mane and A.M. Al-Enizi, in eds.: R.S. Mane and V.V. Jadhav, Types, Synthesis Methods and Applications of Ferrites, In: Spinel Ferrite Nanostructures for Energy Storage Devices, Elsevier, Chap. 4, pp. 51-82 (2020).

2. R. Bharamagoudar, A. Patil, S. Mathad and L. Kankanawadi, *Int. J. Self-Propag. High-Temp. Synth.*, **33**, 165 (2024); https://doi.org/10.3103/S1061386224700110
3. T. Zeeshan, S. Waseem, Z. Ejaz, Z. Kayani and T.E. Kuntsevich, *Inorg. Chem. Commun.*, **162**, 111687 (2024); https://doi.org/10.1016/j.inoche.2023.111687
4. S.V. Rathod, V.U. Magar, S.V. Rajmane, D.R. Sapate and K.M. Jadhav, *J. Mater. Sci. Mater. Electron.*, **36**, 191 (2025); https://doi.org/10.1007/s10854-025-14227-x
5. V.U. Magar, S.V. Rathod, P.S. Patil, S. More and M. Babrekar, *J. Mater. Sci. Mater. Electron.*, **35**, 967 (2024); https://doi.org/10.1007/s10854-024-12705-2
6. I. Hossain, M.T. Islam, N.M. Sahar, M. Samsuzzaman, A. Alzamil and M.S. Soliman, *J. Sci.: Adv. Mater. Dev.*, **9**, 100750 (2024); https://doi.org/10.1016/j.jsamd.2024.100750
7. H.L. Andersen, C. Granados-Miralles, K.M.Ø. Jensen, M. Saura-Múzquiz and M. Christensen, *ACS Nano*, **18**, 9852 (2024); https://doi.org/10.1021/acsnano.3c08772
8. M.A. Rafiq, A. Javed, M.N. Rasul, M.A. Khan and A. Hussain, *Ceram. Int.*, **46**, 4976 (2020); https://doi.org/10.1016/j.ceramint.2019.10.237
9. W. Mansouri, F. Hcini, S. Hcini, A.H. Alshehri, F. Bahri, S. Bouzidi, J. Dhahri, T. Guerfel and M.L. Bouazizi, *J. Mater. Sci. Mater. Electron.*, **33**, 23468 (2022); https://doi.org/10.1007/s10854-022-09107-7
10. U. Ahmad, M. Afzia, F. Shah, B. Ismail, A. Rahim and R.A. Khan, *Mater. Sci. Semicond. Process.*, **148**, 106830 (2022); https://doi.org/10.1016/j.mssp.2022.106830
11. S. Joshi, M. Kumar, S. Chhoker, G. Srivastava, M. Jewariya and V. Singh, *J. Mol. Struct.*, **1076**, 55 (2014); https://doi.org/10.1016/j.molstruc.2014.07.048
12. R.S. Yadav, I. Kuřitka, J. Vilcakova, P. Urbánek, M. Machovsky, M. Masař and M. Holek, *J. Phys. Chem. Solids*, **110**, 87 (2017); https://doi.org/10.1016/j.jpcs.2017.05.029
13. S. Verma, A. Maurya, H. Verma, R. Singh and B. Bhoi, *Chem. Phys. Impact*, **9**, 100674 (2024); https://doi.org/10.1016/j.chphi.2024.100674
14. P.S. Patil, Y.P. Ubale, S.S. Gawali, M.R. Pai and K. Jadhav, *Ceram. Int.*, **50**, 54155 (2024); https://doi.org/10.1016/j.ceramint.2024.10.272
15. S.S. Roy, Ph.D. Thesis, Synthesis and Characterization of Tin Oxide and Copper Doped Tin Oxide Thin Films by Spray Pyrolysis, Department of Physics, Bangladesh University of Engineering and Technology, Dhaka, Bangladesh (2009).
16. R. Rani, S. Sharma, M. Quaglio, S. Hernandez, S. Bianco, A. Chiodoni, and C.F. Pirri, in eds.: R. Rai, Fabrication of KNN Thin-Films *via* a Spin Coating Technique, In: Smart Materials for Smart Living, Nova Science Publishers INC., India, Chap. 9, p. 277 (2017).
17. M.N. Ghazzal, E. Aubry, N. Chaoui and D. Robert, *Beilstein J. Nanotechnol.*, **6**, 2039 (2015); https://doi.org/10.3762/bjnano.6.207
18. E.G. Agbim, I.L. Ikhioya and A J. Ekpunobi, *IOSR J. Appl. Phys.*, **11**, 70 (2019).
19. S.R. Ardekani, A.S.R. Aghdam, M. Nazari, A. Bayat, E. Yazdani and E. Saievar-Iranizad, *J. Anal. Appl. Pyrol.*, **141**, 104631 (2019); https://doi.org/10.1016/j.jaap.2019.104631
20. K. Sasikumar, R. Bharathikannan, G. Sujithkumar, G.J. Arputhavalli, S. Raja, M. Vidhya, R. Marnadu and R. Suresh, *J. Supercond. Nov. Magn.*, **34**, 2189 (2021); https://doi.org/10.1007/s10948-021-05948-1
21. P. Rao, R. Godbole and S. Bhagwat, *Mater. Chem. Phys.*, **171**, 260 (2016); https://doi.org/10.1016/j.matchemphys.2016.01.016
22. M. Vadivel, R. Ramesh Babu and M. Sridharan, *J. Supercond. Nov. Magn.*, **35**, 2563 (2022); https://doi.org/10.1007/s10948-022-06309-2
23. A. Faramawy and H. El-Sayed, *Nano Express*, **4**, 045007 (2023); https://doi.org/10.1088/2632-959X/ad0ee9
24. V.D. Patil, D.A. Patil, A.L. Jadhav, S.L. Jadhav, A.V. Kadam, S.R. Dandwate and B.R. Shinde, *Discover Electrochem.*, **1**, 2 (2024); https://doi.org/10.1007/s44373-024-00003-9
25. V.Y. Popova, V.V. Petrov, A.P. Ivanishcheva and E.M. Bayan, *Funct. Mater. Lett.*, **17**, 2440005 (2024); https://doi.org/10.1142/S1793604724400058
26. K. Tanbir, M.P. Ghosh, R.K. Singh, M. Kar and S. Mukherjee, *J. Mater. Sci. Mater. Electron.*, **31**, 435 (2020); https://doi.org/10.1007/s10854-019-02546-9
27. S.B. Somvanshi, S.A. Jadhav, M.V. Khedkar, P.B. Kharat, S. More and K. Jadhav, *Ceram. Int.*, **46**, 13170 (2020); https://doi.org/10.1016/j.ceramint.2020.02.091
28. S.K. Paswan, S. Kumari, M. Kar, A. Singh, H. Pathak, J. Borah and L. Kumar, *J. Phys. Chem. Solids*, **151**, 109928 (2021); https://doi.org/10.1016/j.jpcs.2020.109928
29. V. Bhuvaneshwari, N. Lenin, C. Shiva, M. Kathirvel, V. Ragavendran, A. Rajeshwari, B. Guruprakash and G.G.V. Kumar, *Mater. Sci. Eng. B*, **288**, 116184 (2023); https://doi.org/10.1016/j.mseb.2022.116184
30. V. Lakhani, T. Pathak, N. Vasoya and K. Modi, *Solid State Sci.*, **13**, 539 (2011); https://doi.org/10.1016/j.solidstatesciences.2010.12.023
31. S.A. Jadhav, M.V. Khedkar, S.B. Somvanshi and K. Jadhav, *Ceram. Int.*, **47**, 28623 (2021); https://doi.org/10.1016/j.ceramint.2021.07.021
32. T. Tatarchuk, M. Myslin, I. Mironyuk, M. Bououdina, A.T. Pędziwiatr, R. Gargula, B.F. Bogacz and P. Kurzydło, *J. Alloys Compd.*, **819**, 152945 (2020); https://doi.org/10.1016/j.jallcom.2019.152945
33. Y.P. Ubale, P.S. Patil, S.S. Gawali, S.K. Modi, K.B. Modi and K.V. Jadhav, *J. Supercond. Nov. Magn.*, **38**, 93 (2025); https://doi.org/10.1007/s10948-025-06935-6
34. M.T. Kotkar, S.M. Wani, P.G. Shinde, A.G. Patil and K.M. Jadhav, *Solid State Commun.*, **400**, 115914 (2025); https://doi.org/10.1016/j.ssc.2025.115914
35. A.R. Chavan, M.V. Shisode, P.G. Undre and K.M. Jadhav, *Appl. Phys., A Mater. Sci. Process.*, **125**, 472 (2019); https://doi.org/10.1007/s00339-019-2768-5
36. A.R. Chavan, S.D. Birajdar, R.R. Chilwar and K.M. Jadhav, *J. Alloys Compd.*, **735**, 2287 (2018); https://doi.org/10.1016/j.jallcom.2017.11.326
37. C. Cherpin, D. Lister, F. Dacquait and L. Liu, *Materials*, **14**, 2557 (2021); https://doi.org/10.3390/ma14102557
38. G. Dixit, J. Singh, R. Srivastava, H. Agrawal and R. Chaudhary, *Adv. Mater. Lett.*, **3**, 21 (2012); https://doi.org/10.5185/amlett.2011.6280